



LTE-based Low-cost and Low-power Soil Moisture Sensing

Yuda Feng

University of Massachusetts Amherst
Amherst, MA, USA
yudafeng@umass.edu

Deepak Ganesan

University of Massachusetts Amherst
Amherst, MA, USA
dganesan@cs.umass.edu

Yaxiong Xie

University at Buffalo, SUNY
Buffalo, NY, USA
yaxiongx@buffalo.edu

Jie Xiong

University of Massachusetts Amherst
Amherst, MA, USA
jxiong@cs.umass.edu

ABSTRACT

Soil moisture sensing is a basic function required by applications like precision irrigation. Recently, RF based soil moisture sensing solutions [10, 43] have been proposed, which, however, can hardly support large scale deployment in challenging outdoor environments, since they must have dedicated signal emitters and also require power supply for either the signal emitters (WiFi or RFID reader) or both the transceivers (WiFi AP and client). LTE signal provides a unique opportunity for soil moisture sensing as the ubiquitously deployed base stations are naturally always-on signal emitters, eliminating the need for deploying extra hardware. In this paper, we implement a low-cost LTE based soil moisture sensor using commercial off-the-shelf hardware. We also realize duty-cycled soil sensing by automatically self-calibrating the phase offset after powering on the devices, significantly reducing the overall power consumption of the sensor. Extensive experiments show that our low-cost sensor (\$55) achieves a high accuracy (3.15%) which is comparable to high-end soil moisture sensors (\$850), wide coverage (2.4 km from the base station) and low power consumption (lasting 16 months using batteries).

CCS CONCEPTS

- Human-centered computing → Ubiquitous and mobile computing systems and tools.

KEYWORDS

LTE sensing, Pervasive sensing, Smart agriculture, Soil moisture sensing, Low-power and low-cost sensing

ACM Reference Format:

Yuda Feng, Yaxiong Xie, Deepak Ganesan, and Jie Xiong. 2022. LTE-based Low-cost and Low-power Soil Moisture Sensing. In *ACM Conference on Embedded Networked Sensor Systems (SenSys '22)*, November 6–9, 2022, Boston, MA, USA. ACM, New York, NY, USA, 14 pages. <https://doi.org/10.1145/3560905.3568525>

Permission to make digital or hard copies of all or part of this work for personal or classroom use is granted without fee provided that copies are not made or distributed for profit or commercial advantage and that copies bear this notice and the full citation on the first page. Copyrights for components of this work owned by others than ACM must be honored. Abstracting with credit is permitted. To copy otherwise, or republish, to post on servers or to redistribute to lists, requires prior specific permission and/or a fee. Request permissions from permissions@acm.org.

SenSys '22, November 6–9, 2022, Boston, MA, USA

© 2022 Association for Computing Machinery.

ACM ISBN 978-1-4503-9886-2/22/11...\$15.00

<https://doi.org/10.1145/3560905.3568525>

1 INTRODUCTION

Measuring the volumetric water content in soil, *i.e.*, soil moisture sensing, is a basic function for diverse applications. For example, agriculture accounts for 70% of the worldwide water usage but wastes over 40% of them [41], so precision irrigation has been proposed to enable sustainable agriculture. Soil moisture sensing is the key enabler of the core task for precision irrigation: having water brought right to the roots of the plants, exactly when the plants need it, and in just the right quantity they need. Soil moisture sensing also plays important roles in hydrology that studies the movement, distribution, and management of water on earth.

Directly measuring soil moisture by removing, drying, and weighing of a soil sample cannot support real-time and *in-situ* measurement. Indirectly measuring the volumetric water content by using some other property of the soil, such as electrical resistance, dielectric constant, or interaction with neutrons, as a proxy for measuring the moisture level has been the main steam design principle of commercial soil moisture sensors. It is, however, challenging to balance the cost and accuracy of the commercial grade soil moisture sensor. Only high-end sensors (sub \$1000) are able to provide accurate estimation results for soil moisture sensing, hindering the deployment in scale.

Recently, RF based soil moisture sensing [10, 43] has been proposed, which leverages the impact of soil moisture level on the property of RF signal, such as the speed [10] or minimum response threshold [43], as the proxy to infer the moisture. RF based solutions significantly reduce the cost and achieve reasonable accuracy at the same time.

The existing RF based solutions, however, have two fundamental limitations. First, a dedicated signal emitter is required, *e.g.*, the WiFi AP or the RFID reader. Due to the limited communication range, the emitter must be densely deployed to cover a wide area, such as the farms or the gardens, resulting in significant implementation cost. Second, current solutions require power supply for the signal emitter (WiFi AP or RFID reader) and the receiver (WiFi client). In the outdoor environment, such as the farms covering a large area, providing power supply for the signal emitter and the signal receiver buried inside soil is extremely challenging. We note that, even though the RFID tag requires no power supply, due to the limited communication range between the reader and tag, the number of required signal emitter (RFID reader) is much larger than WiFi based solutions, making the RFID based solution only applicable to small scale deployment, such as the greenhouse.

The widely deployed LTE infrastructure (base stations) provides a unique opportunity for soil moisture sensing in outdoor environments where power supply becomes challenging:

- **Always-on signal emitters.** The base stations continuously broadcast the cell reference signal and thus naturally serves as an always-on LTE signal transmitter, saving the effort of deploying any extra signal emitters.
- **Wide coverage.** According to the Federal communication market report [5] of the USA, 98% of the population and 84% of areas are covered by LTE networks. The pervasive coverage guarantees that the cellular signal is available even in challenging outdoor environments and thus facilitates wide area deployment in applications like precision irrigation and hydrology.

In this paper, based on our observation, we propose LTE-Soil-Meter—an LTE-based soil moisture sensing system, by leveraging the phenomenon that LTE signals travel slower in soil with higher permittivity (thus higher moisture level) [10]. We have three design objectives for LTE-Soil-Meter: **low cost**, **low power**, and **high accuracy**. First, even though we leverage the cellular base stations as the signal emitters and save huge deployment cost, we still need to further design a low-cost LTE signal receiver and signal processing modules so that we can densely deploy them to cover the large area of farms or gardens. Second, our signal receivers and signal processing modules must consume minimum power and support months- or even years-long operation without replacing battery, after being deployed in challenging outdoor environments. Last but not least, our system should be able to report accurate soil moisture estimation results.

We build a low cost LTE based soil moisture sensor using commercial off-the-shelf hardware. Specifically, we adopt two low-cost SISO software-defined-radio (RTL-SDR [34]) as the RF frontend to collect raw LTE signal and use a Raspberry Pi as the controller to process the received signal and estimate the soil moisture level. By doing so, the total cost of one sensor is kept at \$55.

Atop of our low-cost sensor hardware, we propose to reduce the overall power consumption by adopting duty-cycled sensing schedule, based on the fact that the soil moisture varies slowly during one day. The nature of soil moisture makes the duty-cycled sensing a perfect fit. The existing WiFi based soil moisture sensing system does not implement duty cycle because of practical hardware limitations. Specifically, the frequent powering on and off of the radio chains in duty cycle makes the phase calibration challenging. Typically, to calibrate the phase offset between radio chains, the common practice is to directly connect a dedicated signal transmitter to the receivers via equal length cables. The dedicated signal emitter is removed after deployment. Doing so, however, requires the radio chains to maintain always on, so the phase offset remains constant, which wastes a significant amount of power. Embedding one dedicated transmitter inside the sensor, however, doubles the hardware cost and also drains the battery fast since transmitting RF signal consumes orders of magnitude higher power than purely passive signal receiving.

We propose an automatic phase calibration algorithm that enables low-power duty cycle with minimum hardware cost. We observe that Raspberry Pi is able to output a single-frequency continuous wave via its GPIO interface, and propose to reuse the Raspberry as a signal generator and directly connect the Raspberry Pi and the RTL-SDR receiver. A single tone signal, however, provides no frequency diversity and thus is not enough to remove the phase errors caused by diverse error sources. To fully harness the frequency diversity, we propose a frequency hopping based calibration algorithm via tuning the central frequency of Raspberry Pi generated signal to scan the whole spectrum of the RTL-SDR. Implementing our automatic calibration algorithm only requires two extra low-cost RF switches (\$3.75), introducing minimum overhead.

We implement a prototype of our LTE based soil moisture sensor and evaluate its performance via both in-lab controlled experiments and field tests in the wild. Extensive experiment results demonstrate that our low-cost and low-power sensor (\$55) is able to achieve comparable soil moisture sensing accuracy (mean absolute error of 3.15%) as the high-end commercial sensor (\$850). Our field tests also prove that our sensor works robustly under diverse types of soil, e.g., grass covered soil, potting mix soil, sandy loam or even stony ground. The measurement of the power consumption shows that our sensor is able to work continuously for 16 months without the need to replace batteries.

We summarize the main contributions of our work as follows:

- We for the first time propose to exploit LTE signals for soil moisture monitoring. By leveraging the inherent advantages of wide coverage and extensive existing infrastructure, we move one big step towards large-scale real deployments.
- We implement our soil moisture monitoring system using commercial off-the-shelf devices and at the same time meeting the requirements of low cost, lightweight and low power. We enable low-power duty cycles with minimum extra cost, by leveraging the existing hardware resources and LTE signal properties.
- We implement our design and demonstrate the effectiveness of our LTE-based soil moisture monitoring system. Extensive experiments show that our system achieves a high accuracy (3.15%), which is comparable to high-end soil moisture sensors (\$850), wide coverage (2.4 km from the base station) and low power consumption (lasting 16 months).

The rest of this paper is organized as follows. We introduce the necessary background of RF-based soil moisture sensing and LTE operation in §2. We introduce the detailed design of our sensor in §3 and cover the implementation details in §4. We evaluate the performance of the proposed sensor in §5, survey the related works in §6 and discuss the possible limitations in §7. At last, we conclude our paper in §8.

2 BACKGROUND

In this section, we introduce the key rationale of the RF-based soil moisture sensing and the necessary background of LTE physical layer signal structure.

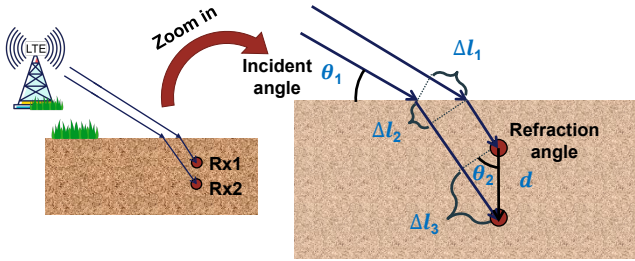


Figure 1: Signal propagation path traveling through air and soil.

2.1 Primer on RF-based Soil Moisture Sensing

The volumetric water content \mathcal{M} (or the soil moisture) is the ratio of the volume of water to the unit volume of soil, which affects the dielectric permittivity ϵ of the soil. Prior study [42] has derived the empirical relationship between the soil moisture and the dielectric permittivity:

$$\mathcal{M} = 0.1138\sqrt{\epsilon} - 0.1758. \quad (1)$$

On the other hand, the dielectric permittivity of soil determines the speed of electromagnetic wave c inside the soil: $c = c_0/\sqrt{\epsilon}$, where c_0 represents the speed of electromagnetic wave in the air. As a result, we could estimate the soil moisture as:

$$\mathcal{M} = 0.1138 \cdot \frac{c_0}{c} - 0.1758. \quad (2)$$

According to above equation, soil moisture monitoring requires accurate measurement of the speed of RF wave inside the soil.

TDoF-based moisture sensing. Ideally, we are able to calculate the speed of RF wave given the traveling distance l and the *Time-of-Flight* (ToF) τ . Highly accurate ToF estimation, however, demands ultra-wide bandwidth and tight synchronization between the RF transceivers, imposing stringent hardware requirements. To enable low-cost RF based soil moisture sensing, *Time-Difference-of-Flight* (TDoF) based sensing methods [10] have been proposed. As shown in Figure 1, the TDoF $\Delta\tau$ of the signals arriving at two antennas is:

$$\Delta\tau = \frac{\Delta l_3}{c} + \frac{\Delta l_2}{c} - \frac{\Delta l_1}{c_0} = \frac{\Delta l_3}{c} + \frac{\Delta l_2}{c} - \frac{\Delta l_1}{\sqrt{\epsilon} \cdot c}. \quad (3)$$

According to the geometric relationship between the *incident angle* θ_1 and the *refraction angle* θ_2 , we have:

$$\Delta l_1 = \frac{\cos \theta_1}{\cos \theta_2} \Delta l_2. \quad (4)$$

Meanwhile, according to Snell's law [44], we have:

$$\sqrt{\epsilon} = \frac{\cos \theta_1}{\cos \theta_2}. \quad (5)$$

Combining Eqn. 3, 4, and 5, we obtain the speed of RF wave in soil:

$$c = \frac{\Delta l_3}{\Delta\tau} = \frac{d \sin \theta_2}{\Delta\tau} \quad (6)$$

where d is the distance of two receiving antennas and thus is a known constant. Ideally, the refraction angle θ_2 is also known if the sender and receiver locations are known. (we relax this requirement in §3.4). To estimate the speed c of RF wave in soil, we only need to measure the TDoF $\Delta\tau$ of signals arriving at two antennas, which can be obtained by calculating the phase difference of signals received at the two antennas [10].

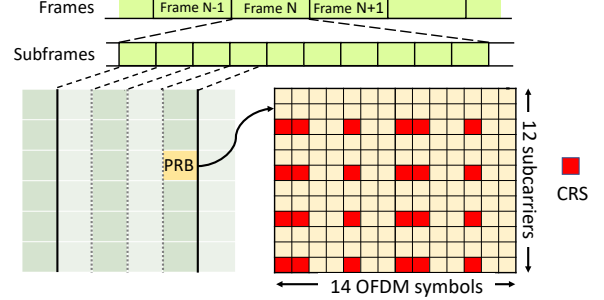


Figure 2: LTE divides time into 10-millisecond radio frames, which are further divided into subframes. LTE groups 14 OFDM symbols and 12 subcarriers into one PRB. Cell reference signal (CRS) scatters inside the resource elements of each PRB.

2.2 LTE Primer

In LTE, the transmissions are organized into 10-millisecond *radio frames*, just as shown in Figure 2. Each radio frame is further divided into 10 one-millisecond *subframes*. LTE adopts OFDMA in the physical layer and allocates 14 OFDM symbols inside each subframe. LTE divides the frequency into 15 kHz subcarriers. The resource block consisting of one subcarrier in frequency and one OFDM symbol in time is one *resource element*. LTE groups 14 OFDM symbols in time (1 subframe) and 12 subcarriers in frequency as one Physical Resource Block (PRB). LTE selects a set of predefined *cell reference signal* (CRS) for channel estimation and transmits them inside a predefined set of resource elements in each PRB, just as shown in Figure 2. We note that, one resource element is empty if it is not used for transmitting data, but the base station continuously broadcasts the CRS even when all the other resource elements are empty.

An LTE receiver is able to estimate the channel state information (CSI) using the received CRS. We denote $X(l, k)$ as the transmitted known reference signal, and $Y(l, k)$ to represent the received reference signal at the l -th OFDM symbol and k -th subcarrier, the CSI $H(l, k)$ can then be calculated as:

$$H(l, k) = \frac{Y(l, k)}{X(l, k)} = \alpha \exp(-j2\pi \frac{d}{\lambda}) + n(l, k) \quad (7)$$

where α denotes the complex attenuation in the propagation, d denotes the path length traveling from the LTE base station to the receiver, λ is the wavelength of the signal, and $n(l, k)$ denotes noise. As shown in Figure 2, the LTE receiver first estimates CSI of the l -th OFDM symbol and the k -th subcarrier that contains reference signals (CRS), and then interpolates across time and frequency to obtain the full CSI matrix.

3 DESIGN

We now introduce the design of our LTE based soil moisture system. We begin with the introduction of the low-cost hardware implementation, followed by the description of the low-power duty cycle algorithm. At last, we introduce the detailed soil moisture estimation algorithm using our low-cost and low-power sensor.

3.1 Low-cost Hardware Architecture

Figure 3 depicts the hardware architecture of the proposed soil moisture sensor. We use two low-cost SISO software-defined-radio (RTL-SDR at \$16) [2] as the front end to receive the raw LTE signals, which are connected to a Raspberry Pi Zero 2W (\$15) [29] via USB interfaces. The Raspberry Pi demodulates the LTE signal, estimates the CSI and estimates the soil moisture. The overall hardware cost is only 47 dollars (total cost increases to \$55 after adding two RF switches (\$3.75) in §3.3).

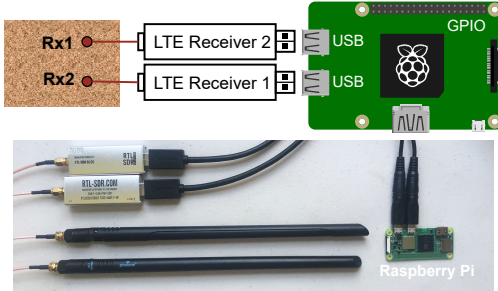


Figure 3: Main components of our low-cost hardware system.

Bandwidth mismatch. We choose RTL-SDR because of its low cost. The cost, in turn, limits the capability of the hardware. Specifically, the RTL-SDR only supports 2.5 MHz signal bandwidth, while the bandwidth of the LTE base stations are much wider (typical bandwidth is 5, 10 and 20 MHz). Performing tight synchronization and accurately estimating the signal phase of the wide-band signal using receivers with limited bandwidth are challenging.

Our key observation is that, different from traditional wireless systems (e.g., WiFi, RFID and LoRa) that transmits preambles that occupy the full channel bandwidth for synchronization, LTE transmits *primary synchronization signal* (PSS) and *secondary synchronization signal* (SSS) for synchronization and both of them only occupy the central 1.4 MHz, as shown in Figure 4. We, therefore, set two RTL-SDRs to the same central frequency as the base station and extract the corresponding PSS and SSS signals for synchronization. By doing so, we could achieve the same level of synchronization as the wide-band hardware. After synchronization, we derive the CSI using the cell reference signal received within the central 2.5 MHz [12] and calculate the phase difference of CSI measured from two RTL-SDRs to estimate the soil moisture.

3.2 Signal Alignment across RTL-SDRs

The two RTL-SDRs are unsynchronized with each other and perform independent synchronization with the base station. We need to align the signal received from two RTL-SDRs before we can leverage their phase difference for soil moisture estimation. We propose a two-phase signal alignment algorithm: a coarse-grain IQ sample alignment followed by a fine-grain OFDM symbol level phase alignment.

3.2.1 Sample level alignment. We leverage the physical layer structure of LTE to perform signal alignment. LTE signals are transmitted in frames, which consist of 140 OFDM symbols, and the frame information is encoded on the central 1.4 MHz of the OFDM symbols

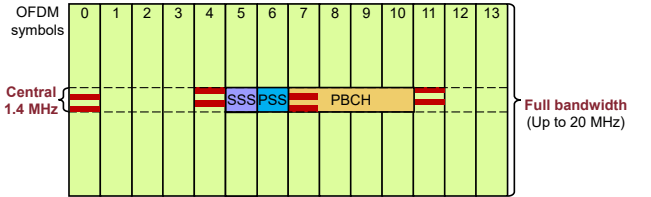


Figure 4: The central 1.4 MHz contains the PSS and SSS signal, which are used for synchronization, and the PBCH channel that contains the index of the radio frames.

as shown in Figure 4. The base station numbers every frame and broadcasts the index of each frame via the physical broadcast channel (PBCH) of that specific frame. After synchronization, the LTE receiver identifies the boundary of each frame and segments the received signal into frames accordingly.

We observe that, the PBCH also resides inside the central 1.4 MHz of every LTE channel with arbitrary channel bandwidth, so the frame index inside the PBCH can be decoded using a 2.5 MHz RTL-SDR receiver. We, therefore, align the frames received from two RTL-SDRs according to the decoded frame index and thus automatically align the samples inside each frame.

3.2.2 Phase alignment within each OFDM symbol. In the conventional MIMO devices, all the radio chains are driven by the same clock source, so they are sharing the same carrier frequency offset (CFO), sampling frequency offset (SFO) and sampling timing offset (STO). When calculating the phase difference of signals received by multiple radio chains, all the CFO, SFO and STO are automatically canceled out [10]. However, in our multi-receiver system, two SISO RTL-SDRs driven by two independent clock sources have different CFO, SFO and STO. Therefore, we need to align the phase and mitigate the effect of aforementioned hardware errors before calculating the accurate phase difference.

Model of phase difference. The impact of CFO, SFO, STO and carrier phase offset (CPO) on the phase of signal received from an individual radio chain (or receiver) has been extensively studied in prior works such as [46]. Accordingly, we model the CSI phase difference $\Delta\Phi_{l,k}$ of the k -th subcarrier and the l -th OFDM symbol received from two RTL-SDRs as:

$$\Delta\Phi_{l,k} = 2\pi f_{TX}\Delta\tau + \Phi_{CPO} + l\Phi_{CFO} + lk\Phi_{SFO} + k\Phi_{STO} \quad (8)$$

where $2\pi f_{TX}\Delta\tau$ denotes the target phase rotation caused by the TDoF, f_{TX} is the frequency of the transmitted signal, and Φ_{CPO} , Φ_{CFO} , Φ_{SFO} , Φ_{STO} represent the unit errors caused by the difference of CPO, CFO, SFO and STO between two RTL-SDRs. We could observe that the error introduced by CFO changes with time (or l), the error introduced by STO changes with frequency (or k) and the error introduced by SFO changes with both time and frequency (l and k). We summarize the properties of all the phase components of Eqn. 8 in Table 1.

Error estimation and correction. Supposing the LTE channel consists of K subcarriers and we receive L OFDM symbols, then we would obtain a matrix of phase difference, i.e., $\Delta\Phi_{l,k}$, where $l = [1, \dots, L]$ and $k = [1, \dots, K]$. We first eliminate all the frequency invariant components by subtracting between adjacent

Table 1: Properties of all the phase components in the phase difference of received signals from two RTL-SDRs.

	Time invariant	Time variant
Frequency invariant	Target phase rotation + Carrier phase offset	Carrier frequency offset
Frequency variant	Sampling timing offset	Sampling frequency offset

phase difference elements along the frequency domain:

$$\Delta\Phi_{l,k+1} - \Delta\Phi_{l,k} = l\Phi_{SFO} + \Phi_{STO}, \quad (9)$$

Afterwards, we cancel the time invariant STO by subtracting adjacent phase difference elements along the time domain:

$$(\Delta\Phi_{l+1,k+1} - \Delta\Phi_{l+1,k}) - (\Delta\Phi_{l,k+1} - \Delta\Phi_{l,k}) = \Phi_{SFO} \quad (10)$$

Till now, we derive the impact of ϕ_{SFO} . We also note that, by performing the above operation on the matrix of size $K \times L$, we obtain $(L - 1) \times (K - 1)$ estimations of the same ϕ_{SFO} . We calculate the mean of all these estimations as our final estimation to minimize the effect of the random noise caused by the environment, measurement, thermal effect, and so on. Substituting the estimated Φ_{SFO} in Eqn. 9, we could obtain the estimation of Φ_{STO} .

Similarly, we calculate the difference of the phase difference along the time domain and obtain:

$$\Delta\Phi_{l+1,k} - \Delta\Phi_{l,k} = \Phi_{CFO} + k\Phi_{SFO}. \quad (11)$$

We then estimate the Φ_{CFO} by subtracting the estimated Φ_{SFO} from the above equations. In total, we obtain $(L - 1) \times K$ estimations of Φ_{CFO} after performing the above operations over the matrix of phase difference, and use their mean value as our final estimation.

After compensating CFO, SFO, STO, we have the only phase offset CPO left. However, both the target phase rotation and CPO are fixed along the time and frequency domain. It is not able to differentiate them from each other. An CPO calibration at the initialization stage is required to eliminate CPO before extracting the target phase rotation for soil sensing. To calibrate CPO, the conventional method is to leverage a known transmitter sending known signals through two cables with equal lengths [46]. Under such a circumstance, the $\Delta\tau = 0$ and the target phase rotations is zero in the matrix of phase difference $\Delta\Phi_{l,k}$. CPO becomes the only unknown in the matrix and thus can be accurately estimated.

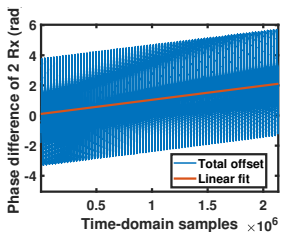


Figure 5: Oscillating phase offset riding on the other phase offsets.

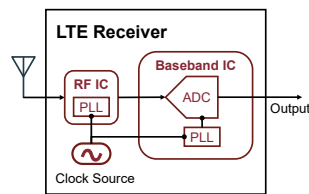


Figure 6: Hardware architecture of the RTL-SDR with two main components.

3.2.3 Oscillating phase offset. Except the phase error caused by the CFO, CPO, SFO, and STO, we also observe a unique oscillating phase offset in the phase difference of signals received from two RTL-SDRs, just as shown in Figure 5.

Root cause. We conduct a series of experiments to find the root cause of the oscillating phase offset. The radio chain of RTL-SDR consists of two separate signal processing integrated circuit (IC): the RF processing IC and the baseband processing IC, just as shown in Figure 6. These two ICs have their own phase-locked-loop (PLL). According to the source code of the driver program [31], RTL-SDR implements a *direct baseband receiving mode*, which supports bypassing the RF processing IC and directly feeding signals to the baseband processing IC. We, therefore, set two RTL-SDRs in the direct baseband receiving mode, feed the same signal to the baseband IC and calculate the phase difference. We plot the results in Figure 7, from which we could see that the baseband IC is not the source of the oscillating phase offset.

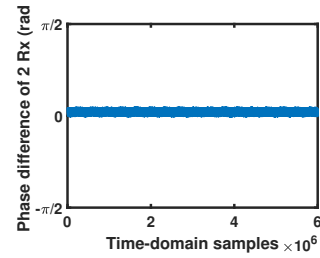


Figure 7: Phase difference of 2 Rx directly through baseband IC (passing by RF IC).

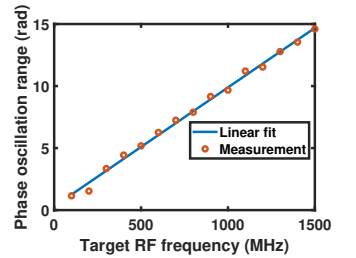


Figure 8: Phase oscillation range versus the target RF frequency setting in the PLL.

We then feed the RF signal into the RF IC, independently adjusting the parameters of the RF-domain processing including the sampling rate, RF gain, central frequency, and check whether the oscillating phase offset will be affected. We observe that the phase oscillation range is proportional to the RF PLL frequency [32], as shown in Figure 8. For our LTE receivers in the frequency band of 700-800 MHz, the oscillation range is in the range of 7-8 rad.

The RF PLL is highly likely the root cause of such an oscillating phase offset. Ideally, RF PLL should generate stable frequency outputs, but in reality it always oscillates near the target frequency to realize a dynamic frequency lock, causing a time variant phase offset. The two RTL-SDRs use separate PLLs in their RF IC. In the initialization stage, their outputs lock to two random frequency offset. As a result, two unaligned oscillating outputs lead to the oscillating phase difference between the two receivers.

Error handling. It is hard to accurately model the oscillating phase offset, but we have two observations that help remove it from phase difference. First, periodicity in time. The oscillating phase varies periodically in the time domain. We plot one cycle of the varying phase in Figure 9. We also perform spectral analysis on the isolated oscillating phases, and plot the results in Figure 10, from which we see that the main frequency component is at 48.55 Hz and thus the oscillating period is 20.6 ms, which is very stable according to our empirical data. The shape of the phase curve also maintains the same within one cycle. The only property that varies is the difference between the peak and valley, which is determined by the RF

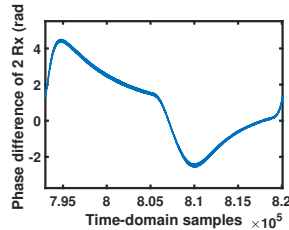


Figure 9: One cycle of the oscillating phase offset in the time domain.

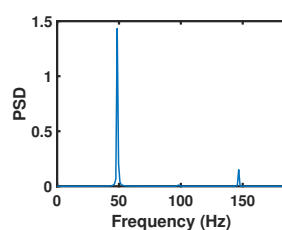


Figure 10: Spectrum analysis to find the period of the PLL caused oscillating phase offset.

PLL frequency, as shown in Figure 8. Second, frequency invariance. The oscillating phase has the same pattern on all the subcarriers. According to the above analysis, we see that the oscillating phase is time variant but frequency invariant, which is the same as the CFO, indicating that the CFO we estimated includes two components, just as shown in Figure 5. We note that the phase error caused by CFO is linear while the oscillating phase is nonlinear. Thus, we separate the CFO via linear regression. The residual phase is the oscillating phase and can be removed from the phase difference.

3.3 Low-power Duty Cycle

To reduce the overall power consumption of our system, we propose to adopt duty cycle based sensing scheduling, based on the fact that the soil moisture changes slowly (in hours).

Challenge. Duty-cycled soil moisture measurement is a common practice for commercial soil sensors to save energy. It is, however, challenging to be directly implemented on existing WiFi based soil moisture sensing systems [10]. Duty cycle requires frequent powering on and off. Every time we power on the RF radio chain, the CPO is randomly initialized. As we have mentioned in §3.2.2, to estimate the CPO, we need to perform an off-line calibration by directly connecting one dedicated RF transmitter to the receiver. Typically, the dedicated RF transmitter is removed after deployment [10, 46]. But, by doing so, we must turn on the RF receiver to maintain the CPO value, contradicting the requirement of the duty cycle operation. If we embed one dedicated signal emitter in soil moisture sensor purely for calibration purpose, the hardware cost almost doubles. More importantly, the power consumption increases significantly, since transmitting RF signals consumes orders of magnitude higher power than purely passive reception, which also conflicts with the purpose of low-power duty cycle.

3.3.1 Automatic calibration. We propose an automatic calibration solution without adding any additional signal emitter, based on two key observations. First, unlike the dedicated WiFi or LTE network interface card that can only process standard WiFi or LTE signals, the RTL-SDR in our system can be programmed to process arbitrary signals. Second, the Raspberry Pi can be programmed to be a signal generator. Specifically, the Raspberry Pi has an internal integrated clock to drive its CPU, which is able to generate a continuous wave with a central frequency smaller than 1.5 GHz. The range of the central frequency perfectly covers the band of LTE base stations we choose in our implementation (700-800 MHz). More importantly, we can program the Raspberry Pi to set the central frequency and

output it using the GPIO port. We note that setting the central frequency does not affect the frequency of the CPU. Based on our observations, we propose to feed the continuous wave generated by the Raspberry Pi into the RTL-SDRs to calibrate the CPO.

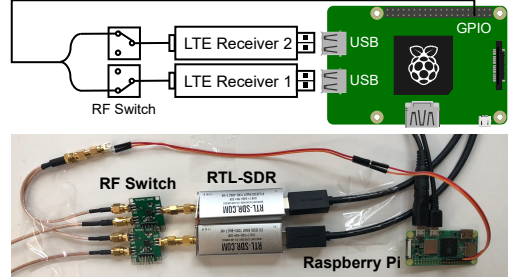


Figure 11: Illustration of the calibration circuit.

Hardware configuration. To realize our idea, we connect the GPIO port of the Raspberry Pi to two low-cost (\$3.75) RF switches [9] via equal-length cables, just as shown in Figure 11. We also connect the LTE antennas to the other ports of the RF switches to receive LTE signals. We program the Raspberry Pi to control the switches to receive calibration signals from its own GPIO during the calibration stage, and to receive LTE signals from the LTE antennas during the soil moisture measuring stage.

Frequency hopping based data sampling. We need to estimate the impact of CFO, SFO, and STO, before we can calibrate the CPO. By receiving the known single-frequency signals generated by the Raspberry Pi, we can only estimate the CSI of a single frequency (similar to one subcarrier). However, according to Eqn. 8, we need CSI measurements across frequencies to estimate and then mitigate the impact of those frequency variant phase errors.

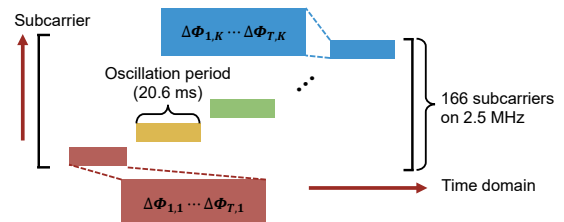


Figure 12: Scheduling the frequency hopping based data sampling.

To obtain CSI measurements across frequencies, we propose a frequency hopping based data sampling algorithm during the phase calibration process. As shown in Figure 12, we first configure the Raspberry Pi to generate a signal at the k -th frequency (subcarrier), at which we measure T CSIs within a period of 20.6 ms. We then program the Raspberry Pi to switch the central frequency of the generated signal and repeat the CSI measurement process. There are 166 subcarriers within the bandwidth of the Raspberry Pi (2.5 MHz). Scanning all the subcarriers takes about 3.4 seconds, given the sampling time at each subcarrier is 20.6 ms. To reduce the time spent on the initial calibration and thus save the energy, we only collect CSI on six subcarriers that are symmetric to the central

subcarrier (see §5.2), with a gap of 28 subcarriers between each two adjacent subcarriers.

Phase error correction. We denote the phase difference of the T CSIs collected from the k -th subcarrier of two RTL-SDRs as:

$$\Delta\Phi_k^T = \begin{bmatrix} \Delta\Phi_{1,k} \\ \Delta\Phi_{2,k} \\ \dots \\ \Delta\Phi_{T,k} \end{bmatrix} \quad (12)$$

where the phase difference $\Phi_{t,k}$ can be calculated according to Eqn. 8. Accordingly, the phase differences of all the sampled CSIs are given as:

$$\Delta\Phi = [\Delta\Phi_1^T, \Delta\Phi_2^T, \dots, \Delta\Phi_K^T] \quad (13)$$

where $K = 6$ in our current implementation, since we only sample in six pre-selected subcarriers.

We follow similar steps described in §3.2.2 to estimate and eliminate the impact of CFO, STO and SFO. Specifically, we first subtract the adjacent phase difference along the time dimension and obtain:

$$\Delta\Phi_{t+1,k}^T - \Delta\Phi_{t,k}^T = \Phi_{CFO} + l\Phi_{SFO}. \quad (14)$$

We then subtract the phase difference in the frequency dimension:

$$(\Delta\Phi_{t+1,k+1}^T - \Delta\Phi_{t,k+1}^T) - (\Delta\Phi_{t+1,k}^T - \Delta\Phi_{t,k}^T) = \Phi_{SFO}. \quad (15)$$

By doing so, we isolate the Φ_{SFO} , and obtain $T \times (K - 1)$ noisy estimations of Φ_{SFO} . We use the mean value of all those estimations as our final result. By subtracting the estimated Φ_{SFO} in Eqn. 14, we obtain the estimated Φ_{CFO} . We note that, Φ_{CFO} represents the phase difference caused by two CFOs between the transmitter and two RTL-SDR. Since the CFO induced phase error is linear, the final CFO included phase difference is determined by:

$$(f_{tx} - f_{rx_1}) - (f_{tx} - f_{rx_2}) = f_{rx_1} - f_{rx_2}. \quad (16)$$

Therefore, even though we change the transmitting frequency, the introduced Φ_{CFO} is the same across different subcarriers (transmitting frequencies). By removing Φ_{CFO} and Φ_{SFO} from Eqn. 13, only Φ_{CPO} and Φ_{STO} are left. Since Φ_{STO} is frequency variant while Φ_{CPO} is frequency invariant, we can estimate the Φ_{STO} first by subtracting adjacent phase differences in frequency dimension and at last estimate the Φ_{CPO} , as we have done in §3.2.2.

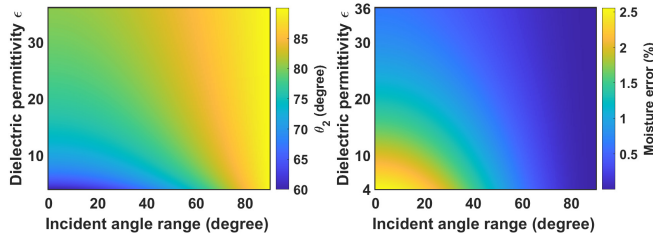


Figure 13: The possible range of unknown θ_2 .

Figure 14: The possible moisture error when assuming $\theta_2 = 90^\circ$.

3.4 Soil Moisture Estimation

Unknown base station locations. When calculating the speed c in Eqn. 6, we assume that the refraction angle θ_2 can be calculated using the locations of the base stations. However, knowing the exact locations of all the deployed sensors and all the base stations is a strong assumption, which may not be valid in real world deployment. We now describe how to realize soil moisture estimation without knowing the base station locations.

According to Snell's law [44], we can calculate the refraction angle θ_2 as:

$$\theta_2 = \arccos\left(\frac{\cos\theta_1}{\sqrt{\epsilon}}\right). \quad (17)$$

We plot all possible value of θ_2 in Figure 13, given that the common range of ϵ varies in [4, 36] for soil [10], and the incident angle may vary in the range $[0^\circ, 90^\circ]$, from which we could see that the range of θ_2 is within $[60^\circ, 90^\circ]$, much smaller than the value space of θ_1 . In our implementation, we directly set the $\theta_2 = 90^\circ$.

We now analyze how much error is introduced to the final moisture estimation by using the fixed θ_2 value. We denote the dielectric permittivity for $\theta_2 = 90^\circ$ as ϵ_{est} . Given Eqn. 6 and $\epsilon = (c_0/c)^2$, we have $\epsilon_{est} = \epsilon \sin^2 \theta_2$. The possible soil moisture estimation error between the assumption ϵ_{est} and the actual ϵ is obtained by Eqn. 1:

$$\begin{aligned} \Delta M &= 0.1138\sqrt{\epsilon}(1 - \sin\theta_2) \\ &= 0.1138\sqrt{\epsilon}\left(1 - \sin\arccos\left(\frac{\cos\theta_1}{\sqrt{\epsilon}}\right)\right). \end{aligned} \quad (18)$$

The moisture error due to the setting $\theta_2 = 90^\circ$ is shown in Eqn. 18, which is determined by the real incident angle θ_1 and the real dielectric permittivity ϵ . We obtain the possible error distribution in Figure 14. The max soil moisture error caused by our assumption is about 2.5% at the bottom left corner of the error map, and the mean moisture error is about 0.7%. The maximum error occurs when the actual dielectric permittivity $\epsilon = 4$ and the actual incident angle $\theta_1 = 0^\circ$ (actual $\theta_2 = 60^\circ$). To compute the mean error, we let both the incident angle and the dielectric permittivity change at a step of 0.01. We compute all the corresponding moisture errors ΔM , and then we compute the average, which is about 0.7%, remaining in an acceptable error range.

Subcarrier combination. We obtain one estimation of the soil moisture using the calibrated CSI from each subcarrier. To effectively combine the estimations from all the subcarriers, we need to analyze the credibility of the estimations on different subcarriers, i.e., the impact of errors on different subcarriers.

We only analyze the impacts of SFO and STO on different subcarriers, since CFO, CPO and the oscillating phase offset have the same impact across subcarriers. After OFDM demodulation, different subcarriers fall on different baseband frequencies from $\pm\Delta f$ to $\pm(K/2)\Delta f$, where Δf denotes the LTE subcarrier bandwidth, i.e., 15 kHz. Due to SFO, there is a time error in each sample interval, i.e., $1/\hat{f}_s - 1/f_s$, where f_s represents the ideal sampling frequency after compensating SFO and \hat{f}_s represents the actual sampling frequency with SFO, just as shown in Figure 15. For a subcarrier at the frequency of $k\Delta f$, the time delay causes a phase error:

$$\Delta\phi = 2\pi k\Delta f \left(\frac{1}{\hat{f}_s} - \frac{1}{f_s}\right). \quad (19)$$

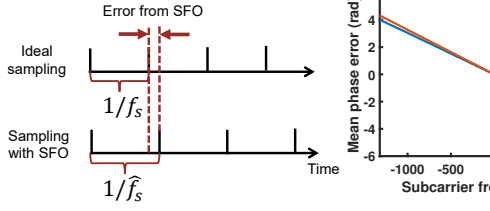


Figure 15: Illustration of SFO caused error.

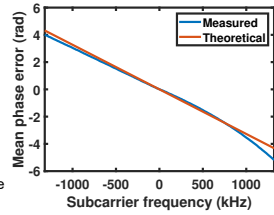


Figure 16: SFO caused phase error caused in one sample interval.

In the above equation, $\frac{1}{f_s} - \frac{1}{\hat{f}_s}$ is the same for any subcarriers, while $k\Delta f$ varies across subcarriers, which indicates that, given a certain SFO, a higher subcarrier frequency results in a larger phase error in the same interval. Figure 16 shows both the theoretical (from Eqn. 19) and experimental phase errors for different subcarrier frequencies in one sample interval, which matches with our analysis. Based on the above conclusion, we set lower weights ($1/k\Delta f$) to the subcarriers with higher frequencies and compute the weighted soil moisture estimation as the final output.

4 IMPLEMENTATION

Software implementation. We implement the LTE demodulation procedure and a real-time LTE CSI tool in C++. Our minimal LTE CSI tool works on lightweight, low-cost and low-power devices. Table 2 shows the comparison between our LTE CSI tool and the widely used WiFi CSI tools [13, 16]. All of them realize the basic functions including real-time reception and demodulation, saving CSI to files for future use and real-time CSI visualization facilitating research. However, our CSI tool provides more than 5.6x CSI readings than the WiFi CSI tools. To accelerate execution, we also provide two levels of parallelization of the computation: multi-threading [23] and offloading the channel estimation tasks to GPU using OpenCL [15]. [7] demonstrates the real-time CSI demodulation and visualization using our LTE CSI tool. And [8] presents another real-time hand speed estimation demo requiring heavy computation (threefold auto-correlation).

Microbenchmark. We obtain an quantified computational complexity comparison of the average CPU usage by letting the programs run on the same PC (Intel® Celeron® Processor J1900, 2.0 GHz). To enable a fair comparison, we let the WiFi CSI tool [16] use two receiver antennas and set the packet rate to 2500 units per second. Also, we reduce the LTE CSI extraction rate to 2500 units per second. We let both programs run for 30 seconds and repeat for 10 times. The average CPU usage for our LTE CSI tool is 5.5%, while the counterpart of the WiFi CSI tool is 33.7%. In conclusion, our LTE CSI tool is much more lightweight than the WiFi CSI tool.

LTE frequency band selection. LTE communication includes a wide range of frequency bands from sub-GHz to 6 GHz, which gives us the freedom to choose the best one for sensing. Wireless signal attenuation in the soil is frequency-dependent [22], and higher frequencies have higher attenuation. So we choose the sub-GHz frequency bands. In our implementation, we choose base stations with central frequency in the range of 700-800 MHz, which are the

Table 2: Functionality comparison between our LTE CSI tool and existing open-source WiFi CSI tools.

Functionalities	LTE CSI tool	WiFi CSI tools
Real-time reception	Enabled	Enabled
Saving to a file		
Real-time visualization		
Max sampling rate	14000 Samples/s	~2500 Samples/s
Computational complexity	Lightweight	heavy duty
GPU acceleration	Enabled	No supported yet

most common sub-GHz bands in the US. There are usually multiple LTE frequency bands provided by different vendors.

Setting the distance between antennas. The distance between two receiving antennas is required to calculate the speed of RF wave inside soil, according to Eqn. 6. Since we calculate the TDoF using the phase difference of signals received at two antennas ($\Delta\tau = \Delta\phi/(2\pi f)$), we have to limit such a phase difference within 2π to eliminate any phase ambiguity. According to Eqn. 6, we calculate the phase difference as:

$$\Delta\phi = 2\pi f \Delta\tau = 2\pi f \frac{\epsilon d \sin \theta_2}{c_0}. \quad (20)$$

Accordingly, by limiting the phase within 2π , we have:

$$d < \frac{c_0}{\epsilon f \sin \theta_2}. \quad (21)$$

The common range of ϵ is 4 to 36 in soil moisture estimation [10]. Given the central frequency range of 700-800 MHz, we obtain the upper bound of the distance $d < 9.37 \text{ cm}$.

The distance is also lower bounded by several factors. First, to deal with the non-homogeneity of the soil, the antenna distance Δd should be large enough to achieve stable results. Second, closely-placed antennas suffer from mutual coupling effects [38], which introduces an additional phase rotation and thus affects the TDoF estimation. Based on extensive experiments (§5.3), we set the antenna distance to 4 cm, which optimizes the performance.

5 EVALUATION

In this section, we evaluate the accuracy of our system. We present the end-to-end evaluation of the soil moisture estimation accuracy (§5.1), followed by a micro-benchmark to investigate the impact of different factors on the accuracy of soil moisture estimation (§5.2). Finally, we evaluate the power consumption of our system (§5.3).

Setup. In our lab experiments, We use a large plastic box as the soil container, just as shown in Figure 17. We place two antennas horizontally in the soil at a depth of 7 cm (the typical insertion depth of high-end sensors [18]) and set the antenna distance d to 4 cm. We set calibration duration to be 0.125 s and the LTE signal collecting duration to be 2 s. We precisely control the water added to the soil and use the ratio of water to the total volume of soil and water as the groundtruth. In our field experiments, we use the same antenna configurations as lab experiments and use the soil moisture measured with a high-end commercial soil sensor [18] as the groundtruth.

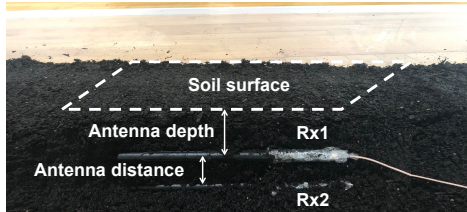


Figure 17: Laboratory setting overview.

5.1 Soil Moisture Estimation Accuracy

In this section, we first evaluate the overall accuracy of our system using a set of controlled lab experiments. We then perform field tests to investigate the performance of LTE-Soil-Meter in the wild.

Overall accuracy. We first evaluate the accuracy of our system and compare the performance with the high-end soil sensor (\$850) and another low-end soil sensor [17] (\$50). We conduct controlled experiments in the lab to accurately control the moisture. Specifically, we change the soil moisture level from 0% to 50% at a step size of 5% and then measure the soil moisture using our LTE based sensor, the high-end and the low-end sensor, respectively. We repeat the experiments at each moisture level 50 times.

We plot the estimation error in Figure 18, from which we see that the mean estimation errors are 3.15%, 2.50% and 9.38%, for our system, the high-end and low-end commercial soil sensors, respectively. Our system achieves three times higher accuracy than the low-end sensor at similar prices. Compared with the high-end sensor which is ten times more expensive, our system achieves comparable accuracy.

We also observe that, when the soil moisture is lower than 20%, the estimation error of our system decreases with the increase of soil moisture, which matches the result in Figure 14. When the soil moisture is higher than 40%, the effects of signal attenuation caused by high soil moisture gradually become noticeable. Higher attenuation leads to decreased signal-to-noise ratio at the receiver, and accordingly higher error in soil moisture estimation.

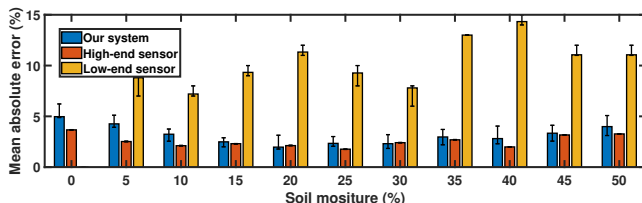


Figure 18: Mean absolute error at different soil moisture levels.

Soil type. To investigate the effect of soil diversity, we conduct experiments with four different types of soil (see Figure 19) in a residential house backyard: the potting mix, the soil with grass covered, the sandy loam, and the stony ground. We conduct experiments at five different locations with one pit shown in Figure 20 for each soil type to avoid bias.

Figure 21 plots the absolute estimation errors measured in four types of soil. We see that the mean estimation errors for the plant covered soil and the potting mix are 3.18% and 2.94% respectively.



(a) Grass covered (b) Potting mix (c) Sandy loam (d) Stony ground

Figure 19: Different soil types in field experiments.

These results demonstrate that the grass covering the soil surface has negligible effect on soil moisture estimation. Our system achieves the lowest mean error and the least deviation in the sandy loam, which is actually the most common field soil in our geographic area. Last but not least, we observe that the small stones on the ground have a noticeable impact on the performance. One possible reason is that stones may cause an extra phase change, degrading the sensing performance.



Figure 20: A pit dug for experiments.

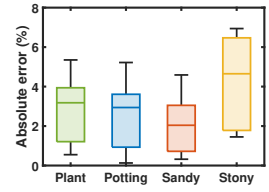


Figure 21: Effects of different ground types.

Types of covering plants. We evaluate the performance of our system in soil that is covered by three types of plants, *i.e.*, flowers, grass, and trees. As shown in Figure 22, the flower stems are around 50 cm long, and the surface of the soil is about 3 meters below the tree crown. Figure 23 shows the performance in these scenarios. Dense flowers increase the mean error by 0.5%, and also result in larger variations of soil moisture estimation. A possible reason is that the flowers are not still and the swinging leaves affect signal propagation, leading to a slightly larger error. As a comparison, the trees also slightly affect the accuracy.



Figure 22: Types of plant covering scenarios. Left: flower bed ; right: under tree.

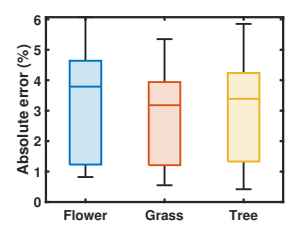


Figure 23: Effects of different covering plants on soil moisture estimation.

Distance to the base station (Soil sensing coverage). We now evaluate the soil sensing range with respect to the LTE base stations,

i.e., the sensing coverage in downtown and suburban areas. In the downtown experiments, We evaluate the moisture sensing accuracy by varying the distance between the LTE base station and receiver from 200 m to 1200 m at a step size of 200 m. For each distance, we randomly pick five locations to evaluate the performance of soil moisture sensing. For experiments in the suburban area, we vary the distance from 400 m to 2400 m at a step size of 400 m.

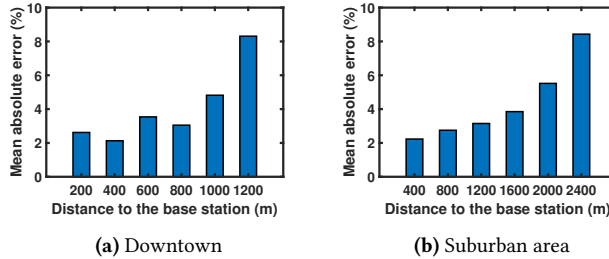


Figure 24: Effects of distance to the base station.

We plot the soil moisture estimation errors in Figure 24a. We see from the figure that, due to signal attenuation and complex multipath in the downtown area, the estimation error increases with distances, but not monotonically. Even when the distance is 1200 m, the soil moisture estimation error (8%) is still lower than the low-end commercial soil sensor [17]. Note that the radius of the communication coverage of a downtown LTE base station is about 1 km [11]. Figure 25a shows the real coverage on the map, in which LTE soil sensing covers all of the downtown area and part of our university at the northwest corner. In the suburban area, the estimation error increases monotonically with the distance. The moisture sensing error is still reasonably low (8%) at a distance of 2400 m, demonstrating a larger sensing range in open areas. Figure 25b shows the farm fields within the sensing coverage.

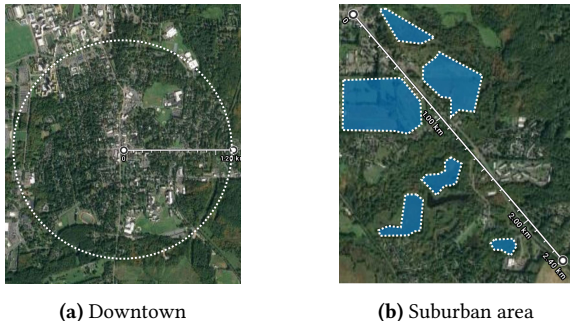


Figure 25: Sensing coverage on the map, blue areas represent the farm fields within the sensing coverage.

Compared with the existing WiFi based solution [10] and RFID-based solution [43], the proposed LTE-based system achieves a sensing coverage hundreds of times larger, moving a big step towards large-scale deployments in real-world scenarios.

Times of day and weather. We observe that the LTE signal quality is affected by the times of day (*i.e.*, daytime or night) and weather. To quantify their impacts on soil moisture sensing, we conduct

experiments at different times of day and under varying weather conditions. In each experiment, the LTE receivers are placed at the same location. For times of day, we collect data in the daytime and in the night separately for five continuous days. For varying weather conditions, we collect data under four different weather conditions, *i.e.*, sunny, cloudy, windy and rainy. We average 20 measurements for each setup.

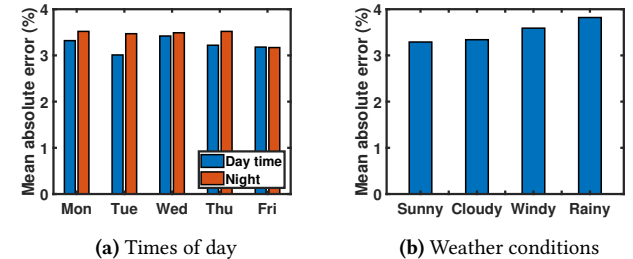


Figure 26: Effects of times of day and weather conditions.

We could see from Figure 26a that on average, the soil moisture error at night is 0.2% higher than that in the daytime. A possible reason is that the LTE base stations switch to power-saving mode [45] during nights when there are fewer users. The lower signal strength results in lower SNR and slightly affects the sensing performance. On the other hand, we could see from Figure 26b that weather conditions do have a noticeable impact on the sensing performance. Specifically, the mean absolute error in rainy days is 0.53% higher than that in the sunny days.

Long-term performance evaluation. To evaluate the long-term performance of our system, we deploy our system in the sandy loam to measure the soil moisture. We also deploy another high-end soil moisture sensor and use its measurements as the ground-truths. We configure both sensors to measure the soil moisture once per hour and plot the measured results in Figure 35. We see that the proposed system works robustly and reports accurate soil moisture levels during the process of the seven-day experiment.

5.2 Micro-benchmarks

We perform micro-benchmarks to evaluate the impact of various factors on the final moisture estimation accuracy.

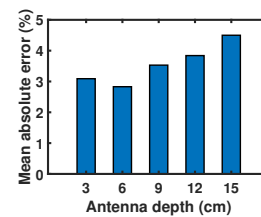


Figure 27: Effects of different antenna depths.

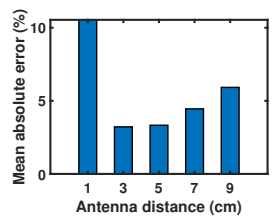


Figure 28: Effects of different antenna distances.

Antenna depth. The antenna depth represents the distance between the soil surface and the upper antenna, just as shown in Figure 17. We vary the antenna depth from 3 cm to 15 cm at a step

size of 3 cm and test the soil moisture sensing accuracy. We repeat the experiments by varying the soil moisture levels from 5% to 45% at a step size of 10%. We plot the results in Figure 27, from which we see that the mean estimation error increases with the antenna depth, *i.e.*, from 2.83% to 4.50%. The main reason is that when the antennas are buried deeper in the soil, the signal attenuation is higher and lower signal-to-noise ratio (SNR) leads to larger error.

Antenna distance. We investigate the impact of antenna distance d on the estimation accuracy. Since we have derived the upper limit (9.37 cm) for the antenna distance in §4, we vary the antenna distance d from 1 cm to 9 cm at a step size of 2 cm. For each distance d , we conduct experiments at five different moisture levels (5% to 45% at a step size of 10%). The average errors are plotted in Figure 28. We see from the figure that, when the two antennas are close to each other (1 cm), the sensing error is larger than 10%. The root cause of this high error is the mutual coupling effects between antennas. With a larger separation between antennas, the mutual coupling effect is greatly mitigated and the error drops significantly. We however note that the error also increases slightly with the distance d (5% at 9 cm). We believe both the larger signal attenuation at the deeper antenna and the varying soil moisture in a larger range contributes to the increased errors. In summary, a distance between 3 cm and 5 cm achieves the best sensing performance and we therefore choose $d = 4$ cm in our implementation.



Figure 29: Two different types of LTE antennas.

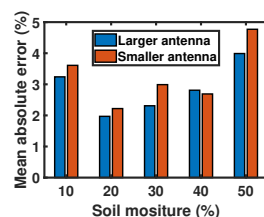


Figure 30: Mean absolute error with different antenna size.

Antenna size. To investigate the impact of the antenna size, we conduct an experiment using two antennas with different sizes but a similar gain of 8 dBi, as shown in Figure 29. We conduct controlled experiments in the lab to accurately control the moisture. We change the soil moisture level from 10% to 50% at a step size of 10% and repeat the experiments at each moisture level for 50 times. Figure 30 shows the results. We observe a very small increase of error when the small antenna is adapted.

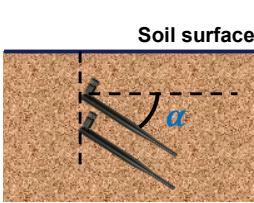


Figure 31: Illustration of the angle between antennas and the soil surface.

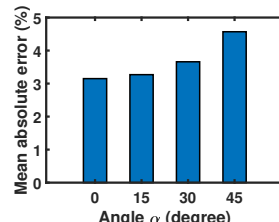


Figure 32: Effects of different angles on soil moisture estimation.

Angle between the antennas and the soil surface. In real deployments, it is hard to place the antennas parallel to the soil surface. We denote the angle between the antennas and the soil surface as α (shown in Figure 31), and evaluate the effect on soil moisture estimation. Specifically, for all tested angles, we keep the vertical distance (*i.e.*, depth difference) of the two antennas as 4 cm. During the experiments, we change α from 0° to 45° . For each setting, we compute the average error on five moisture levels from 5% to 45%. As shown in Figure 32, larger angle α leads to a slightly higher error. In conclusion, an angle less than 30° between the antennas and the soil surface is suggested, which is easy to achieve in real deployments.

Calibration duration. In the calibration process, the number of subcarriers is far more than the number of phase offsets to be computed. So we do not need frequency hopping on all the subcarriers. On the other hand, less hopping leads to less calibration time. We now evaluate the effect of different calibration durations, *i.e.*, the number of hopping subcarriers. We change the calibration time from 0.041 second to 0.250 second, *i.e.*, the number of hopping subcarriers from 2 to 12. For each setting, we evaluate the average error on five moisture levels from 5% to 45%. Figure 33 shows that longer calibration duration leads to higher accuracy. From 0.041 second to 0.125 second, the average accuracy increases by about 1.5%. Further increasing the duration only leads to subtle performance improvement. We therefore set the calibration duration as 0.125 second (6 hopping subcarriers) to balance accuracy and latency.

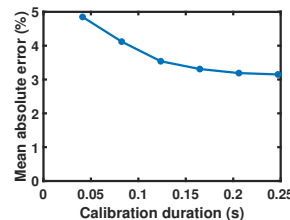


Figure 33: Effects of different calibration duration on soil moisture estimation.

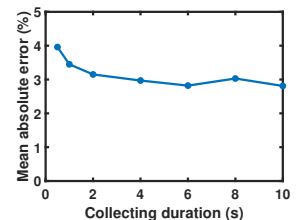


Figure 34: Effects of different data collecting duration on soil moisture estimation.

Data collection duration. The received data is affected by random noise from the environment, thermal effects, etc. We need to receive a certain amount of data to mitigate the issue of noise. In this part, we evaluate the effect of different durations of LTE signal collection (excluding the calibration duration). We evaluate on five moisture levels from 5% to 45% and compute the average moisture error to avoid bias. Figure 34 shows that longer data collection tends to stabilize the estimation results and leads to a slightly higher accuracy. However, extending the collection duration would increase the power consumption and shorten the operational life. When we increase the data collection duration from 0.5 second to 2 seconds, the average accuracy increases by around 1%. We also observe that further increasing the duration does not help improve the sensing accuracy much. We therefore set 2 seconds as the data collection duration in our experiments to maintain a balance between accuracy and power consumption.

5.3 Power Consumption Measurement

We now investigate the power consumption of our soil moisture sensor. We interconnect a USB power source with our system through a USB power meter [25]. We use the USB power meter to measure the power consumption of each component in our sensor.

Table 3 shows the power consumption in one duty cycle. The LTE receivers collect 2-second data to mitigate the effect of random noise and improve the robustness in estimating hardware-caused offsets. The collected data is processed in real time. The reason for the much longer total time is the boot-up and shutdown time of the Raspberry Pi. The total energy consumption for one measurement cycle is 5.385 mWh.

Table 3: Power consumption of the main components and the whole system in one duty cycle.

	Raspberry Pi	LTE receiver	Whole System
Mean power (W)	1.071	1.412	1.583
Working time (s)	12.245	2.191	12.245
Energy (mWh)	3.644	0.865	5.385

Based on the power consumption of one cycle, we calculate the total work time of our sensor without replacing battery and plot the results in Figure 36. We see that, when we set the cycle length to two hours, our system can work over 16 months with 4 common rechargeable batteries (1.5 V and 5000 mAh). In comparison, the WiFi-based system [10] uses a laptop to work with the commercial WiFi chip, which incurs a much higher cost and also a much larger power consumption.

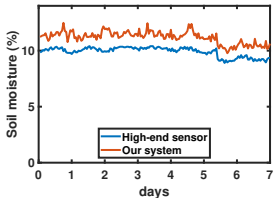


Figure 35: Long term experiment comparison in seven days.

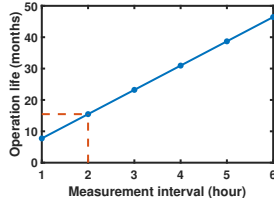


Figure 36: Battery life at different measurement intervals.

6 RELATED WORK

LTE-based sensing. LTE signals have been utilized for localization/tracking [21, 28, 36, 37, 47], vehicle detection [35, 39] and human sensing [3, 12, 24]. Applications leveraging the broadcast LTE downlink signals include fingerprint-based localization [21, 28, 47] and tracking [36, 37]. By collecting and analyzing the reflected signals from cars, car type classification [35] and parking monitoring [39] are realized. For human sensing, researchers achieve hand gesture detection [3] and keystroke recognition [24]. Both these systems require strong received signals to work in indoor environments, and they require microcells or high-gain directional antennas to boost LTE signals. In our previous work [12], we resolve the signal strength limitation through delicate signal processing, and realize fine-grained respiration sensing and car speed monitoring across indoor and outdoor environments.

In this work, we for the first time realize LTE-based soil moisture sensing, greatly extending the capability of LTE sensing. More importantly, compared with existing LTE sensing works using expensive equipment (e.g., USRP), we move a big step towards real-world deployments. Our low-cost LTE sensing system facilitates the development of affordable RF sensing on a large scale.

RF-based soil moisture sensing. Researchers have realized soil moisture sensing leveraging different RF technologies. Remote sensing technologies [26] are proposed for coarse regional soil moisture sensing which is suitable for environment monitoring and geographical imaging in a region. But the low spatial resolution makes it not adequate for agriculture applications. Ground penetrating radar (GPR) [20] is another classic method measuring the light speed in soil to estimate soil moisture. This method achieves a high accuracy and high spatial resolution at the cost of using expensive ultra-wideband radars. In recent years, researchers explore low-cost substitutes leveraging commercial wireless technologies such as RFID [30, 43] WiFi [10] and LoRa [48]. RFID-based works measure the signal attenuation affected by different soil moisture levels. WiFi- and LoRa-based works measure the signal speed leveraging available commercial devices. All these systems can only achieve a limited sensing range, preventing them from real-life large-scale deployments. In comparison, our work enables kilometer-level sensing coverage leveraging LTE signals, which is tens to hundreds of times larger than the existing works. What is more, the proposed system removes the requirement of infrastructure deployment, which greatly reduces the cost and effort for real-world deployments. In a most recent work [19], researchers propose a contactless RF soil moisture sensing method. To achieve accurate ToF measurements for soil moisture sensing, this method requires an expensive SDR [33] (over \$8000) to receive signals on a large GHz-level bandwidth, which is not scalable for real-world deployment. In comparison, the cost of the proposed system is merely \$55.

Soil moisture sensors. Commonly-seen soil moisture sensors include gypsum blocks [6, 40], tension meters [1] and capacitance [14, 27, 27]. Gypsum blocks and tension meters measure the soil tension. When soil water enters the block structures of the sensor, the resistance between the electrodes inside the sensors decreases, and the soil moisture level is indicated by the resistance. The major drawback of these types of sensors is that the effective components decay over time, and thus require a replacement in a few months. Capacitance sensors release an electrical charge into the soil and measure the soil dielectric permittivity. The dielectric permittivity can be mapped to the water volume level in the soil. Capacitance sensors are usually expensive. Our system leverages the RF signal property, *i.e.*, propagation speed in the soil to measure the dielectric permittivity, which facilitates the low-cost realization of soil moisture sensing.

7 DISCUSSION

Indoor soil moisture sensing. Though our system is mainly aiming at outdoor soil moisture monitoring, our system can also support indoor soil moisture sensing. All the experiments under the lab settings are conducted in indoor environments, which validate the effectiveness of the proposed system for indoor soil moisture

sensing. Most greenhouses and balconies are usually surrounded by windows or transparent films, which facilitate the reception of reasonably good quality LTE signals in indoor environments. Thus, our system supports soil moisture monitoring for indoor planting.

Soil moisture higher than 50%. Soil moisture is usually in the range of 5% to 45% [4]. We notice that in some special scenarios such as rice paddy, the moisture level can be higher than 50%. The larger signal attenuation in higher-moisture soil can degrade the sensing performance of the proposed system.

Limitations. Although the proposed system can support kilometer-level coverage leveraging the existing LTE infrastructure covering most of the areas [5], there are still blind spots such as uninhabited farm fields far away from the residential areas. In these areas, commodity LTE extenders could be deployed to facilitate both communication and soil moisture sensing.

8 CONCLUSION

In this paper, for the first time, we realize LTE-based soil moisture sensing. We present the unique advantages of LTE-based sensing including wide coverage and always-on signal emitters, *i.e.*, existing LTE base stations already pervasively deployed. Through extensive experiments, we demonstrate the superior performance of the proposed low-cost and low-power sensing system. We believe this work moves a big step towards real-world adoption of RF sensing for smart agriculture.

ACKNOWLEDGEMENTS

This work was partially supported by the NSF under Grant CAREER-2144668, the CCDC Army Research Laboratory (ARL) under Cooperative Agreement W911NF-17-2-0196 (ARL IoT CRA), and UMass Amherst Institute For Applied Life Sciences (IALS) Equipment Fund.

REFERENCES

- [1] JC Alamillo-Magaña, E Carrillo-Ávila, J Jj Obrador-Olán, C Landeros-Sánchez, J Vera-López, and JF Juárez-López. 2016. Soil moisture tension effect on sugar cane growth and yield. *Agricultural Water Management* 177 (2016), 264–273.
- [2] Aliexpress. 2022. SDR Receiver. Web. <https://www.aliexpress.com/item/3256803544500184.html>
- [3] Weiyan Chen, Kai Niu, Deng Zhao, Rong Zheng, Dan Wu, Wei Wang, Leye Wang, and Daqing Zhang. 2020. Robust dynamic hand gesture interaction using LTE terminals. In *2020 19th ACM/IEEE International Conference on Information Processing in Sensor Networks (IPSN)*. IEEE, 109–120.
- [4] Vasyl Cherlinka. 2018. Soil Moisture: How To Measure & Monitor Its Level. Web. <https://eos.com/blog/soil-moisture/>
- [5] Federal Communications Commission et al. 2020. Communications Marketplace Report.
- [6] B Friis Dela. 2001. *Measurement of soil moisture using gypsum blocks*. SBI forlag.
- [7] For demonstration. 2022. Demo: Hand movement detection. Web. <https://drive.google.com/file/d/1kPVqlL5qwFyoa-V8arOK94psrKzZHVNm/view?usp=sharing>
- [8] For demonstration. 2022. Demo: hand speed estimation. Web. https://drive.google.com/file/d/1D3RL0jO0WwgjTeQ0KIVHQy6_mVsX9yl/view?usp=sharing
- [9] Analog Devices. 2018. HMC349. Web. <https://www.analog.com/en/products/hmc349alp4ce.html#product-overview>
- [10] Jian Ding and Ranveer Chandra. 2019. Towards low cost soil sensing using Wi-Fi. In *The 25th Annual International Conference on Mobile Computing and Networking*. 1–16.
- [11] LTE Encyclopedia. 2022. LTE Radio Link Budgeting and RF Planning. Web. <https://sites.google.com/site/lteencyclopedia/lte-radio-link-budgeting-and-rf-planning>
- [12] Yuda Feng, Yaxiong Xie, Deepak Ganesan, and Jie Xiong. 2021. LTE-based Pervasive Sensing Across Indoor and Outdoor. In *Proceedings of the 19th ACM Conference on Embedded Networked Sensor Systems*. 138–151.
- [13] Jon Gjengset, Jie Xiong, Graeme McPhillips, and Kyle Jamieson. 2014. Phaser: Enabling phased array signal processing on commodity WiFi access points. In *Proceedings of the 20th annual international conference on Mobile computing and networking*. 153–164.
- [14] Manash Protim Goswami, Babak Montazer, and Utpal Sarma. 2018. Design and characterization of a fringing field capacitive soil moisture sensor. *IEEE Transactions on Instrumentation and Measurement* 68, 3 (2018), 913–922.
- [15] Khronos Group. 2018. OpenCL. Web. <https://www.khronos.org/opencl/>
- [16] Daniel Halperin, Wenjun Hu, Anmol Sheth, and David Wetherall. 2011. Tool release: Gathering 802.11 n traces with channel state information. *ACM SIGCOMM computer communication review* 41, 1 (2011), 53–53.
- [17] Xiaomi HHCC. 2022. Flora Monitor. Web. <https://www.giftwows.com/product/flora-monitor/>
- [18] Shun Keda. 2022. Shun Keda TR8D Soil Moisture Tester. Web. <https://www.yoycart.com/Product/671124075629/>
- [19] Usman Mahmood Khan and Muhammad Shahzad. 2022. Estimating Soil Moisture using RF Signals. In *Proceedings of the 28th Annual International Conference on Mobile Computing and Networking*.
- [20] Anja Klotzsche, François Jonard, Majken Caroline Looms, Jan van der Kruk, and Johan A Huisman. 2018. Measuring soil water content with ground penetrating radar: A decade of progress. *Vadose Zone Journal* 17, 1 (2018), 1–9.
- [21] Da Li, Yingke Lei, and Haichuan Zhang. 2020. A novel outdoor positioning technique using LTE network fingerprints. *Sensors* 20, 6 (2020), 1691.
- [22] Li Li, Mehmet C Vuran, and Ian F Akyildiz. 2007. Characteristics of underground channel for wireless underground sensor networks. In *Proc. Med-Hoc-Net*, Vol. 7. 13–15.
- [23] Pthread library. 2004. POSIX thread (pthread) libraries. Web. <https://www.cs.cmu.edu/afs/cs/academic/class/15492-f07/www/pthreads.html>
- [24] Kang Ling, Yuntang Liu, Ke Sun, Wei Wang, Lei Xie, and Qing Gu. 2020. Spider-Mon: Towards using cell towers as illuminating sources for keystroke monitoring. In *IEEE INFOCOM 2020-IEEE Conference on Computer Communications*. IEEE, 666–675.
- [25] MakerHawk. 2004. MakerHawk USB Power Meter. Web. <https://www.amazon.com/dp/B07FMQZVW2>
- [26] Binayak P Mohanty, Michael H Cosh, Venkat Lakshmi, and Carsten Montzka. 2017. Soil moisture remote sensing: State-of-the-science. *Vadose Zone Journal* 16, 1 (2017), 1–9.
- [27] Ekanayaka Achchillage Ayesha Dilrukshi Nagahage, Isura Sumeda Priyadarshana Nagahage, and Takeshi Fujino. 2019. Calibration and validation of a low-cost capacitive moisture sensor to integrate the automated soil moisture monitoring system. *Agriculture* 9, 7 (2019), 141.
- [28] Giovanni Pecoraro, Simone Di Domenico, Ernestina Cianca, and Mauro De Sanctis. 2018. CSI-based fingerprinting for indoor localization using LTE signals. *EURASIP Journal on Advances in Signal Processing* 2018, 1 (2018), 1–18.
- [29] Raspberry Pi. 2018. Raspberry Pi Zero 2 W. Web. <https://www.raspberrypi.com/products/raspberry-pi-zero-2-w/>
- [30] Sérgio Francisco Pichorim, Nathan J Gomes, and John C Batchelor. 2018. Two solutions of soil moisture sensing with RFID for landslide monitoring. *Sensors* 18, 2 (2018), 452.
- [31] pinkavaj. 2022. RTL-SDR diver program. Github. <https://github.com/pinkavaj/rtl-sdr/blob/master/src/librtlsdr.c>
- [32] pinkavaj. 2022. RTL-SDR RF IC driver program. Github. https://github.com/pinkavaj/rtl-sdr/blob/4520f001d85f01d051ea42af7b18b6ef0837e14/src/tuner_r82xx.c#L147
- [33] Ettus Research. 2022. USRP X310. Web. <https://kb.ettus.com/X300/X310>
- [34] RTL-SDR. 2022. RTL-SDR. Web. <https://www rtl-sdr.com/about-rtl-sdr/>
- [35] Santu Sardar, Amit K Mishra, and Mohammed Zafar Ali Khan. 2019. Vehicle detection and classification using LTE-CommSense. *IET Radar, Sonar & Navigation* 13, 5 (2019), 850–857.
- [36] Kimia Shamaei and Zaher M Kassas. 2018. LTE receiver design and multipath analysis for navigation in urban environments. *NAVIGATION, Journal of the Institute of Navigation* 65, 4 (2018), 655–675.
- [37] Kimia Shamaei, Joe Khalife, and Zaher M Kassas. 2018. Exploiting LTE signals for navigation: Theory to implementation. *IEEE Transactions on Wireless Communications* 17, 4 (2018), 2173–2189.
- [38] Hema Singh, HL Sneha, and RM Jha. 2013. Mutual coupling in phased arrays: A review. *International Journal of Antennas and Propagation* 2013 (2013).
- [39] Amala Sonny, Prabhakar Kumar Rai, Abhinav Kumar, and Mohammed Zafar Ali Khan. 2020. Deep learning-based smart parking solution using channel state information in LTE-based cellular networks. In *2020 International Conference on COMmunication Systems & NETworkS (COMSNETS)*. IEEE, 642–645.
- [40] E Stenitzer. 1993. Monitoring soil moisture regimes of field crops with gypsum blocks. *Theoretical and applied climatology* 48, 2 (1993), 159–165.
- [41] High Tide Technologies. 2021. Water Usage In The Agricultural Industry. Web. <https://htt.io/water-usage-in-the-agricultural-industry/#:~:text=As%20previously%20mentioned%2C%2070%25%20of,in%202%20feet%20of%20water>
- [42] G Clarke Topp, JL Davis, and AA P Annan. 1980. Electromagnetic determination of soil water content: Measurements in coaxial transmission lines. *Water resources*

- research 16, 3 (1980), 574–582.
- [43] Ju Wang, Liqiong Chang, Shourya Aggarwal, Omid Abari, and Srinivasan Keshav. 2020. Soil moisture sensing with commodity RFID systems. In *Proceedings of the 18th International Conference on Mobile Systems, Applications, and Services*. 273–285.
 - [44] Wikipedia. 2018. Snell's law. Web. https://en.wikipedia.org/wiki/Snell%27s_law
 - [45] Jingjin Wu, Yujing Zhang, Moshe Zukerman, and Edward Kai-Ning Yung. 2015. Energy-efficient base-stations sleep-mode techniques in green cellular networks: A survey. *IEEE communications surveys & tutorials* 17, 2 (2015), 803–826.
 - [46] Yaxiong Xie, Jie Xiong, Mo Li, and Kyle Jamieson. 2018. mD-Track: Leveraging Multi-Dimensionality in Passive Indoor Wi-Fi Tracking. <https://doi.org/10.48550/ARXIV.1812.03103>
 - [47] Heng Zhang, Zhichao Zhang, Shunqing Zhang, Shugong Xu, and Shan Cao. 2019. Fingerprint-based localization using commercial LTE signals: A field-trial study. In *2019 IEEE 90th Vehicular Technology Conference (VTC2019-Fall)*. IEEE, 1–5.
 - [48] Fusang Zhang Zhaoxin Chang, Junqi Ma Jie Xiong, and Daqing Zhang Beihong Jin. 2022. Sensor-free Soil Moisture Sensing Using LoRa Signals. *Proceedings of the ACM on Interactive, Mobile, Wearable and Ubiquitous Technologies* (2022), 1–25.